

How Are Gamma-Ray Burst Radio Afterglows Populated?

K. Zhang^{1,3}, Z. B. Zhang^{1*}, Y. F. Huang^{2†}, L. M. Song³, S. J. Zheng³, and X. J. Li¹

¹College of Physics and Engineering, Qufu Normal University, Qufu 273165, P. R. China

²School of Astronomy and Space Science, Nanjing University, Nanjing 210023, P. R. China

³Key Laboratory of Particle Astrophysics, Institute of High Energy Physics, Chinese Academy of Sciences, Beijing 100049, P. R. China

Accepted XXX. Received YYY; in original form ZZZ

ABSTRACT

We systematically analyze three GRB samples named as radio-loud, radio-quiet and radio-none afterglows, respectively. It is shown that dichotomy of the radio-loud afterglows is not necessary. Interestingly, we find that the intrinsic durations (T_{int}), isotropic energies of prompt gamma-rays ($E_{\gamma,iso}$) and redshifts (z) of their host galaxies are log-normally distributed for both the radio-loud and radio-quiet samples except those GRBs without any radio detections. Based on the distinct distributions of T_{int} , $E_{\gamma,iso}$, the circum-burst medium density (n) and the isotropic equivalent energy of radio afterglows ($L_{\nu,p}$), we confirm that the GRB radio afterglows are really better to be divided into the dim and the bright types. However, it is noticeable that the distributions of flux densities (F_{host}) from host galaxies of both classes of radio afterglows are intrinsically quite similar. Meanwhile, we point out that the radio-none sample is also obviously different from the above two samples with radio afterglows observed, according to the cumulative frequency distributions of the T_{int} and the $E_{\gamma,iso}$, together with correlations between T_{int} and z . In addition, a positive correlation between $E_{\gamma,iso}$ and $L_{\nu,p}$ is found in the radio-loud samples especially for the supernova-associated GRBs. Besides, we also find this positive correlation in the radio-quiet sample. A negative correlation between T_{int} and z is confirmed to hold for the radio-quiet sample too. The dividing line between short and long GRBs in the rest frame is at $T_{int} \approx 1$ s. Consequently, we propose that the radio-loud, the radio-quiet and the radio-none GRBs could be originated from different progenitors.

Key words: gamma-ray burst: general — radio continuum: transients — radio continuum: individual — methods: data analysis

1 INTRODUCTION

Gamma-Ray Bursts (GRBs) are instantaneous brightening event of gamma rays in the distant universe. After it was reported in 1973 (Klebesadel et al. 1973), a lot of properties of progenitors have been investigated by many previously theoretical and observational researches, see review papers (e.g., Piran 1999; Zhang 2014) for details. Study of GRB afterglows is crucial to understand the central engine and the environment of distinct progenitors. The general interpretation is that a sudden energy release will produce a high temperature fireball expanding at a relativistic speed. The internal dissipation of the fireball leads to the gamma-rays, and the blast wave against the external medium produce the afterglow (Mészáros 2006, Rees & Meszaros 1992, Rees & Meszaros 1994). The hydrodynamic evolution of the jetted outflows from the ultra-relativistic phase to the non-relativistic phase has been studied by a few authors (e.g., Huang et al. 1999, 2003). But there are many questions remaining for GRBs, such as how the inner engine runs, the reason of flares in afterglow and so on (Woosley 1993, Paczynski 1990, Duncan & Thompson 1992, Becerra et al. 2019, Hascoët et al. 2017, Mu et al. 2016). As illustrated in Chandra et al. (2012), the detecting rates of X-ray and optical afterglows are higher than that of radio afterglows.

Due to the relatively longer timescale of radio afterglows, one can have more opportunities to observe the radio afterglows in detail at a later period. In particular, the rebrightening phenomena of some radio afterglows caused by multiple activities of the inner engine of GRBs (Li et al. 2015), energy injection (Geng et al. 2018), supernova (SN) components or the forward and reverse shock can be detected and utilized to constrain the above theoretical rebrightening models. At the same time, the statistical classifications of radio afterglows become more and more important and feasible with the data accumulation of the radio afterglows.

Chandra et al. (2012) sorted 304 GRBs radio afterglows, and found the detection rate to be about 31% that is obviously lower than those of X-ray and optical afterglows even after the *Swift* satellite was launched to detect more X-ray and optical afterglows than before. Also, they sorted radio afterglows at 8.5 GHz for detection and 3σ upper limit between 5 and 10 days and found that there was only little difference between them. The tiny difference was thought to be resulted from the telescope sensitivity (Chandra et al. 2012). However, Hancock et al (2013) pointed out that the instrumental sensitivity was not the intrinsic reason for the difference mentioned above and they found that 60% ~ 70% of the radio selected GRB samples are truly radio bright, while the convinced fraction of the radio faint GRBs is about one third. Chandra et al. (2012) found that there was an apparent correlation between the detectability and the energy of GRBs which may cause the diverse detection rates

* E-mail: astrophysics0817@163.com

† E-mail: hyf@nju.edu.cn

for the radio bright and faint GRB samples. To reduce the influence of many unknown reasons on classifications in terms of the radio brightness, [Lloyd et al. \(2017\)](#) and [Lloyd et al. \(2019\)](#) selected the GRBs with larger isotropic energy ($E_{\gamma,iso} > 10^{52} \text{erg}$) in prompt gamma-rays, and divided them into two sub-samples, that is radio-loud and radio-quiet types. They proposed that the two subsamples might be generated from different progenitors; that is the radio-loud GRBs might be produced from the He-merger while the radio-quiet GRBs may be interpreted by the core-collapse of massive stars.

Owing to the relatively less brightness of GRBs in radio bands, whether the radio afterglows can be classified into any subclasses is still controversial. With the increase of radio afterglow numbers, statistical study becomes more and more reliable and important. Motivated by the above incongruous results, we do a similar analysis but for different samples of GRB radio afterglows in very detail. In addition, we will examine the effects of surrounding mediums and GRB host galaxies on the GRB classifications in radio bands. In order to deduce their potential progenitors, several supernova-associated GRBs with radio afterglow measurements are also included. Simultaneously, we also pay attention to GW170817/GRB170817A detected by Laser Interferometer Gravitational-Wave Observatory (LIGO) and Fermi/Integral satellites ([Goldstein et al. 2017](#); [Savchenko et al. 2017](#)) as the first short GRB associated with Kilonova originated from a binary neutron star merger system ([Abbott et al. 2017](#)).

2 DATA PREPARATION

First of all, we define our sampling criteria in the following: (1) GRBs with radio flux density larger than 3σ error bars constitute the radio-loud sample; (2) those radio afterglows with flux density lower than 3σ levels belong to the radio-quiet (including upper limits) sample; (3) other GRBs without any radio flux detections comprise our radio-none sample. The fact that no radio afterglow is reported (not even an upper limit) for a given burst could be because the telescope was down, or the PI ran out of their budget, or the burst did not fulfill the team's observational criteria which may be a bright optical/X-ray afterglows, or proximity, or something like that. However, each burst involved in our radio-none sample was indeed observed by some radio telescopes or array, but no meaningful flux densities were reported according to [Chandra et al. \(2012\)](#). Most probably, radio afterglows of the radio-none sample could exist but are extremely too weaker to be detected by the current instruments due to sensitivity limits. We choose the GRBs with measured redshift (z) to calculate the intrinsic duration T_{int} and isotropic equivalent energy $E_{\gamma,iso}$ (the intrinsic duration defined as $T_{int} = T_{90}/(1+z)$, where T_{90} is defined as the time that the burst takes from 5 to 95 percent counts of the total gamma-rays, [Kouveliotou et al 1993](#)).

[Chandra et al. \(2012\)](#) reported a large sample of GRB radio afterglows, of which the majority were detected by the Very Large Array (VLA) or Expanded Very Large Array (EVLA), and a small fraction of these radio afterglows were successfully observed by the Australia Telescope Compact Array (ATCA), Westerbork Synthesis Radio Telescope (WSRT), Giant Metrewave Radio Telescope (GMRT) and the Very Long Baseline Array (VLBA). Out of the 304 GRBs in [Chandra et al. \(2012\)](#), we have selected 84 detections and 63 upper limits from the VLA-based afterglows, of which 79 radio-loud, 48 radio-quiet and 25 radio-none bursts with known redshift are involved (hereafter called the VLA-based sample). To compare with the recent high-frequency radio afterglows detected by the Arcminute Microkelvin Imager (AMI) telescope, we have taken 45 de-

tections and 74 upper limits out of 139 bursts at 15.7 GHz from [Anderson et al. \(2018\)](#), from which 21 radio-loud and 34 radio-quiet AMI afterglows with measured redshift are picked out to study the rest-frame features (hereafter called the AMI sample). It is likely that the lower $E_{\gamma,iso}$ bursts in the SN-associated GRB sample are relatively brighter in radio bands in contrast with other bursts. To explore the interesting issue, we have paid particular attention to the SN-associated GRBs and chosen 23 SN/GRBs as a unique subgroup including 21 radio-loud and 2 radio-quiet GRBs. It is noticeable that more than 90 percent of SN/GRB afterglows are radio-loud and the redshifts of all the SN/GRBs in our sample are well known. Moreover, [Lloyd et al. \(2017\)](#) and [Lloyd et al. \(2019\)](#) only chose those energetic bursts with $E_{\gamma,iso} > 10^{52}$ ergs, which will inevitably bias the results of radio quiet afterglows since the $E_{\gamma,iso}$ and radio peak luminosity are positively correlated for different kinds of bursts as described in Sec. 3.6.

All the above samples of radio afterglows are compiled in Tables 1 and 2, in which the key parameters of radio-loud and radio-quiet GRBs are similarly presented. Column 1 gives the name of GRBs; Columns 2 and 3 are respectively the duration (T_{90}) and the redshift (z); In Column 4, we list the k -corrected isotropic energies ($E_{\gamma,iso}$) in γ -ray band; Column 5 gives the medium densities n ; Column 6 provides the spectral peak luminosity ($L_{\nu,p}$) of radio afterglows at a frequency of 8.5 GHz or 15.7 GHz; In Columns 7 and 8, we present the peak radio flux density together 1σ RMS at 8.5 GHz or 15.7 GHz; Column 9 list the radio telescopes which were used to carry out observations; References are given in Column 10. In Table 3, we only provide the values of T_{90} , z , $E_{\gamma,iso}$ and n along with the employed radio telescope in order for the radio-none bursts. If there is no any parameters measured, we just leave them blank. To investigate the properties of host galaxies for different kinds of radio samples, we directly utilize the data of radio flux densities for host galaxies in [Li et al. \(2015\)](#) and [Zhang et al. \(2018\)](#).

3 RESULTS

3.1 Flux density of radio afterglows

We first plot the distributions of radio afterglows for detections and 3σ upper limits between 0 and 10 days at 8.5 GHz in top-left panel of Figure 1, where it is found that our distributions are similar to those in [Chandra et al. \(2012\)](#) and [Hancock et al \(2013\)](#), in which the upper limits are confirmed again to peak at 50-100 μJy in and the detections peaked around 200 μJy with a long extending tail. We also find that there is an obvious truncation at $\sim 400 \mu\text{Jy}$ in the VLA-based detection sample, which motivates us to examine whether the distribution of the flux densities less than 400 μJy is associated with that of the upper-limit sample. For the purpose, we try to define the detection sample whose flux density larger than 400 μJy as radio-loud I sample, and other detections with radio flux density less than 400 μJy to be radio-loud II sample, temporally. It is interestingly found from the bottom panels of Figure 1 that the flux density distributions of radio-loud and radio-quiet AMI afterglows are also bimodally distributed and resemble those of the VLA-based sample. However, the AMI peak flux densities of both detections and upper limits are on average two times larger than those VLA-based ones, correspondingly.

To check if it is necessary to reclassify radio-loud GRBs into two subsamples, we display the cumulative fractions of the intrinsic duration T_{int} and the $E_{\gamma,iso}$ for radio-loud I, radio-loud II and radio-quiet GRBs (upper limits) in Figure 2. As shown in Table 5,

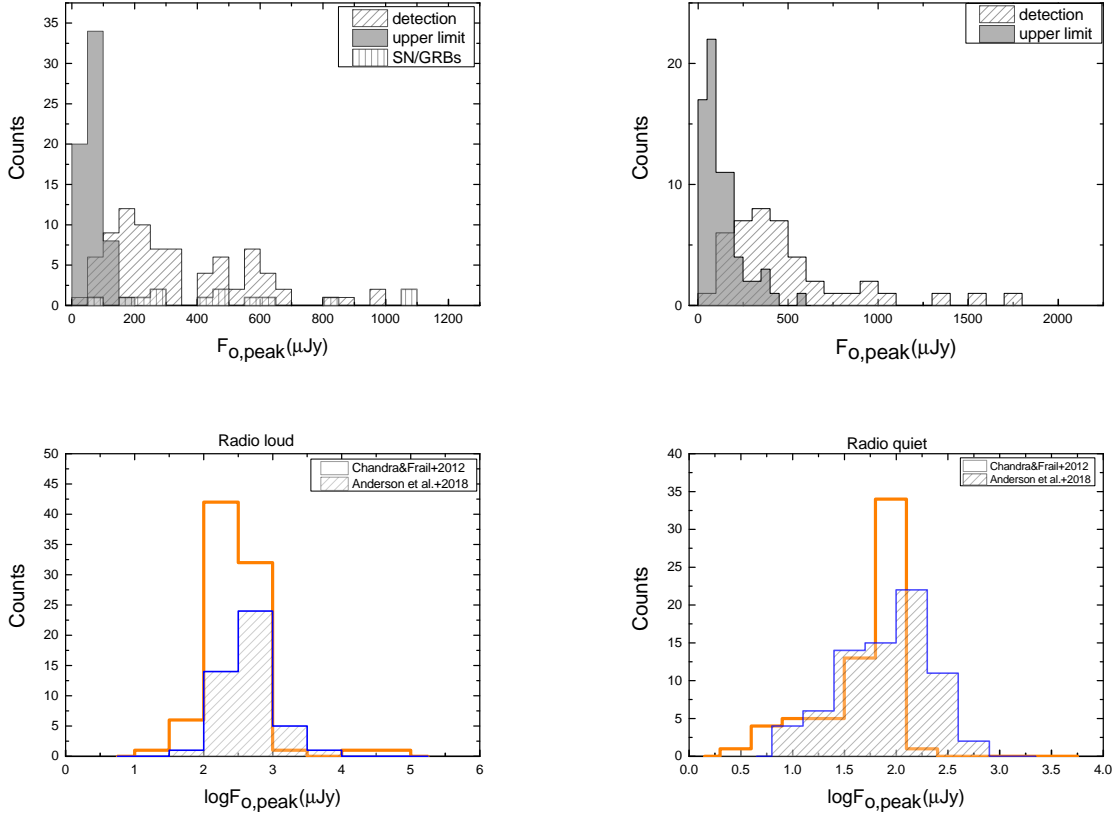


Figure 1. The distributions of peak flux densities for detections and upper limits of radio-loud (filled) and radio-quiet (hatched) afterglows between 0-10 days taken from Chandra et al. (2012) at 8.5 GHz and Anderson et al. (2018) at 15.7 GHz are shown on the top-left and top-right panels, respectively. The vertical shadow on the top-left panel represents the distributional histogram of SN/GRBs. Two bottom panels display the peak flux comparisons of radio afterglows at different frequencies for radio-loud (left) and radio-quiet (right) samples in the logarithmic scale.

the Kolmogorov-Smirnov (K-S) tests return the statistic $D = 0.48$ (0.31) and $P = 7 \times 10^{-4}$ (0.031) between the T_{int} distributions of the radio-loud I (II) and the radio-quiet samples showing the radio-quiet bursts are different from either radio-loud I or II. Similarly, the statistic and p-value of the $E_{\gamma,iso}$ distributions are $D = 0.35$ (0.38) and $P = 0.037$ (0.004) for comparisons between the radio-quiet and the radio-loud I (II) samples. Surprisingly, the K-S test to the radio-loud I and the radio-loud II samples returns $D = 0.27$ with $P = 0.24$ for the T_{int} distribution and $D = 0.14$ with $P = 0.92$ for the $E_{\gamma,iso}$ distribution, indicating that the two radio-loud sub-samples should be taken from the same parent distribution. In other words, dividing radio-loud bursts into two classes is not necessary. Consequently, we shall only investigate the radio-loud, the radio-quiet and the radio-none samples in the subsequent sections, and explore in statistics whether they are basically different kinds of bursts on basis of their observational properties.

3.2 Distributions of z , T_{int} and $E_{\gamma,iso}$ revisited

Using the total sample of 206 GRBs including 151 VLA-based and 55 AMI bursts, we plot the histograms of z , $E_{\gamma,iso}$ and T_{int} for radio-loud, radio-quiet and radio-none samples in Figure A1, where one can find that the distributions of z , T_{int} and $E_{\gamma,iso}$ of radio-loud and radio-quiet samples are well fitted by a gaussian function, but the radio-none sample seems to be eccentric (see Appendix for a detail).

The fitting results are summarized in Table 4, from which we notice that the mean values of z , $E_{\gamma,iso}$ and T_{int} of radio-none GRBs are systematically smaller than those of the other two samples. In particular, the isotropic energies of radio-none bursts are on average one order of magnitude lower than the $E_{\gamma,iso}$ values of either radio-loud or radio-quiet bursts.

Following Hancock et al (2013) and Lloyd et al. (2019), we also analyze the cumulative fractions of the T_{int} and the $E_{\gamma,iso}$ but for different radio-loud, radio-quiet and radio-none VLA-based samples in Figure 3 and Table 5, where we see that the radio-quiet samples are evidently different from the radio-loud ones in terms of the T_{int} distribution, on average the radio-loud GRBs have relatively longer T_{int} as found before (Hancock et al 2013; Lloyd et al. 2019). However, the K-S test demonstrates that the T_{int} distributions of radio-quiet and radio-none GRBs are indistinguishable. Regarding the $E_{\gamma,iso}$ distributions, we also perform the K-S tests to any two of the above three VLA-based samples and find from Table 5 that they are drawn from different parent distributions. In addition, the median discrepancy of $E_{\gamma,iso}$ between the radio-loud and the radio-none bursts is about two orders of magnitude. With the increase of frequency, it is interestingly found that two AMI samples of radio-loud and radio-quiet GRBs at 15.7 GHz are consistent with being drawn from the same parent $E_{\gamma,iso}$ distribution.

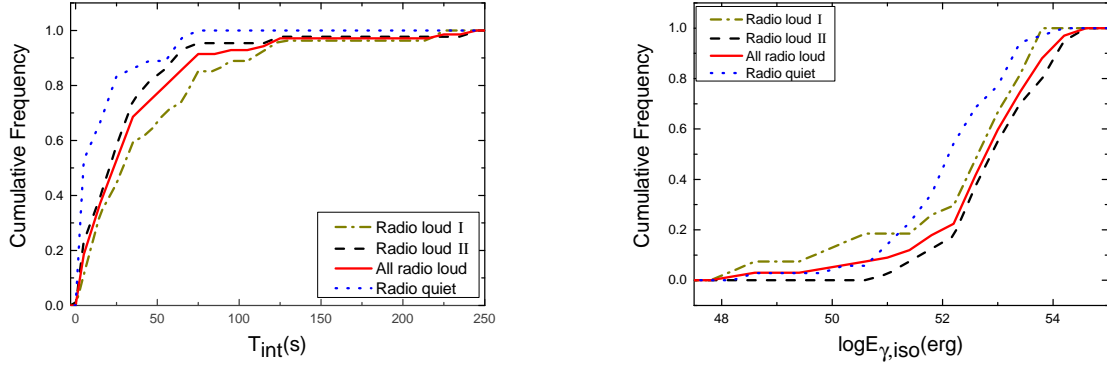


Figure 2. The cumulative fractions of T_{int} and $E_{\gamma,iso}$ are shown for different radio-selected GRBs in left and right panels, respectively.

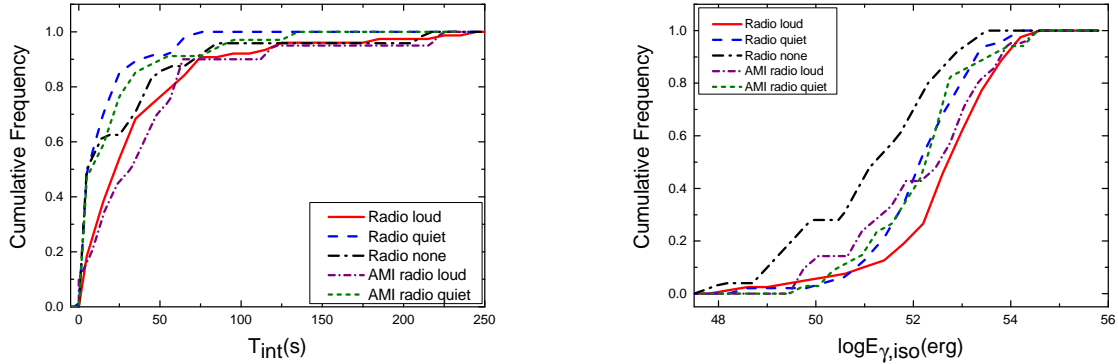


Figure 3. Cumulative fractions of T_{int} (left panel) and $E_{\gamma,iso}$ (right panel) are plotted for the VLA-based radio-loud (red solid line), radio-quiet (blue dashed line), radio-none (black dot-dashed line) bursts and for the AMI Radio-loud (purple short dash-dotted line) and AMI Radio-quiet (green short dashed line) GRBs.

3.3 Radio fluxes of host galaxies

We notice that some GRBs with radio flux densities of host galaxies in Zhang et al. (2018) were not included in our initial radio-loud, radio-quiet or none samples. To increase the reliability in statistics, we assume them to be radio-none or radio-quiet because they don't have radio afterglows detected. In order to analyze the radio flux density of host galaxies for the three samples, we combine the data of radio-none and radio-quiet into a simple radio-faint sample. Then we plot the cumulative fractions for the radio-loud, radio-faint samples in Figure 4 where we find when the radio (flux density of the host galaxies, F_{host}) is less than $50 \mu\text{Jy}$ the radio-loud, the radio-faint samples share the same distribution, but when it is more than $50 \mu\text{Jy}$ the Cumulative fractions of these two samples are significantly different. A K-S test shows that the probability of those two samples from the same distribution is 0.19, so that in terms of host galaxies the two samples might be taken from the same distribution.

Li et al. (2015) found the host flux density F_{host} is positively correlated with the observed peak flux density ($F_{o,peak}$) or the pure flux density ($F_{b,peak}$) of GRBs at a given radio frequency ν as follows

$$F_{host} = (a + b\nu)F_{o,peak}, \quad (1)$$

and

$$F_{host} = \frac{a + b\nu}{1 - (a + b\nu)} F_{b,peak}, \quad (2)$$

where $a \approx 0.3$, $b \approx -0.02$, and $F_{o,peak} = F_{b,peak} + F_{host}$. The Eq. (1) can be used to estimate the host flux density once the peak values of radio afterglows are measured. Figure 5 displays the relationships of F_{host} with $F_{o,peak}$ or $F_{b,peak}$ for the radio-loud and radio-quiet samples. One can find that the radio flux densities of the radio-quiet GRBs and their host galaxies are relatively lower than those of the radio-loud ones. It is noticeable that the very famous nearby short GRB (sGRB) 170817A seen off-axis with an estimated viewing angle of $20^\circ \sim 40^\circ$ (Alexander et al. 2017) is the first electromagnetic counterpart of gravitational-wave event. It has peak flux densities of $\sim 84.5 \mu\text{Jy}$ and $\sim 58.6 \mu\text{Jy}$ observed correspondingly at $\nu = 3 \text{ GHz}$ and 5.5 GHz around 130 days since the merge of double neutron stars (Li et al. 2018). Using the above Eq. (1) and (2), one can easily predict the host flux densities to be about $20.3 \mu\text{Jy}$ at $\nu = 3 \text{ GHz}$ and $11.1 \mu\text{Jy}$ at $\nu = 5.5 \text{ GHz}$. Interestingly, GW 170817/sGRB170817A as a radio-loud burst has relatively weaker radio afterglows and lower host fluxes in contrast with other normal radio-loud GRBs. However, it is located near the radio-quiet bursts as shown in Figure 5, which indicates that galactic types or circum-burst environment of differ-

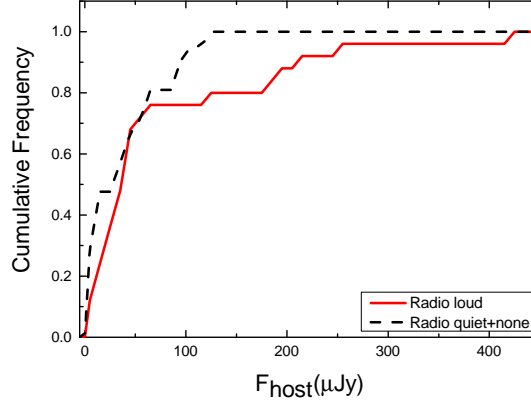


Figure 4. Cumulative fractions of F_{host} for radio-loud (solid red line), radio-faint (black dashed line) samples.

ent radio-selected GRBs could be diverse although their dominant radiation mechanisms might be the same.

3.4 The surrounding medium density

As pointed out by Chandra et al. (2012), the centimeter radio afterglow emission is the brightest for circum-burst densities from 1 to 10 cm^{-3} . Beyond the narrow density range, the flux density will become weak due to either a low intrinsic emission strength (for lower densities) or the increased synchrotron self-absorption (for higher densities). From the literatures, it is well known that the circum-burst medium densities (n) of GRBs usually span several orders of magnitude and are hard to be determined (e.g. Wijers & Galama 1999; Chandra et al. 2012; Fong et al. 2015; Zhang et al. 2018). In our samples, the circum-burst densities are distributed in a fairly wide scope spanning ~ 10 orders of magnitude seen from Table 1 to 3. Because the number of radio-quiet GRBs with estimated densities is extremely limited, we thus combine the radio-quiet and the radio-quiet samples into a newly-formed radio faint sample in order to increase the statistical confidence level. Then we plot the cumulative fractions for the two samples in Figure 6 and apply a K-S test to get $D=0.55$ with a probability of 0.002, which demonstrates that the radio-loud and radio faint samples are significantly incongruous with each other. In contrast, the medium densities of the radio-loud host galaxies are relatively larger than those of the radio faint ones. Furthermore, the fraction of low densities of $n \leq 0.1 \text{ cm}^{-3}$ for the radio faint sample is around six times more than that for the radio-loud sample. On the contrary, about 90 percent of radio-loud afterglows are surrounded by relatively denser mediums of $n \approx 10^{-1} - 10^2 \text{ cm}^{-3}$.

3.5 Spectral luminosity of radio afterglows

We utilize all the GRBs with measured isotropic γ -ray energy instead of $E_{\gamma,iso} > 10^{52}$ (Lloyd et al. 2019) only to ensure our samples to be as complete as possible. Simultaneously, we calculate the spectral peak luminosity at radio band ($L_{\nu,p}$) for the radio-loud and the radio-quiet (or upper limit) samples as (Zhang et al. 2018)

$$L_{\nu,p} = 4\pi D_L^2 f_{m,radio} (1+z)^{-1} k, \quad (3)$$

where $f_{m,radio}$ denotes the peak flux density $F_{o,peak}$ of the radio-loud afterglows or the upper limits of radio-quiet afterglows, k is a K -

correction factor determined by

$$k = (1+z)^{\alpha-\beta}, \quad (4)$$

where $\alpha \sim 0$ and $\beta \sim 1/3$ are assumed to be the normal temporal and spectral indexes, respectively. D_L denoting the luminosity distance of a burst is given by

$$D_L = cH_0^{-1}(1+z) \int_0^z dz' [(1+z')^3 \Omega_M + \Omega_\Lambda]^{-1/2}, \quad (5)$$

in which $c=3.0 \times 10^8 \text{ m/s}$ is the speed of light, H_0 is the Hubble constant taken as 70 km/s/Mpc , other cosmological parameters $\Omega_M=0.27$ and $\Omega_\Lambda=0.73$ have been assumed for a flat universe (Schaefer 2007). Consequently, the $L_{\nu,p}$ values can be obtained from Eq. (3) for the VLA-based GRBs at 8.5 GHz since most afterglows were detected at this frequency. For the AMI bursts reported in Anderson et al. (2018), their $L_{\nu,p}$ values are calculated at a frequency of 15.7 GHz. Owing to lack of measurement of the radio afterglows with the upper limits, the $L_{\nu,p}$ values of radio-quiet afterglows can be only estimated as the upper limits too. Figure 7 displays the $L_{\nu,p}$ distributions of radio-loud, radio-quiet and SN-associated GRBs respectively. On average, the peak luminosity of radio-loud bursts is relatively larger than the other two, while the mean values of radio-quiet and SN-associated GRBs are comparable. The cumulative fractions of all the above samples are shown in Figure 8. A K-S test to them shows that the luminosity distributions of radio-loud and radio-quiet GRBs are largely different for the VLA-based samples since $D=0.4$ ($>D_{\alpha=0.05}=0.25$) with $P \approx 6.6 \times 10^{-5}$ and are however consistent with each other for the AMI samples. It needs to be emphasized that the distributional consistency of $L_{\nu,p}$ for different kinds of radio-selected GRBs is similar to that of the $E_{\gamma,iso}$ distributions in Figure 3. Moreover, the actual deviation between them would become more significant since the accumulative line of the radio-quiet sample consisted of the upper limits should move leftward in a certain sense. The median $L_{\nu,p}$ of radio-quiet sample is about one order of magnitude smaller than that of radio-loud sample. Interestingly, this is similar to the one order of magnitude difference between radio fluxes of host galaxies and GRB afterglows (Zhang et al. 2018). Hence, we conclude that the majority of radio-quiet emissions should be contributed by their surrounding host galaxies.

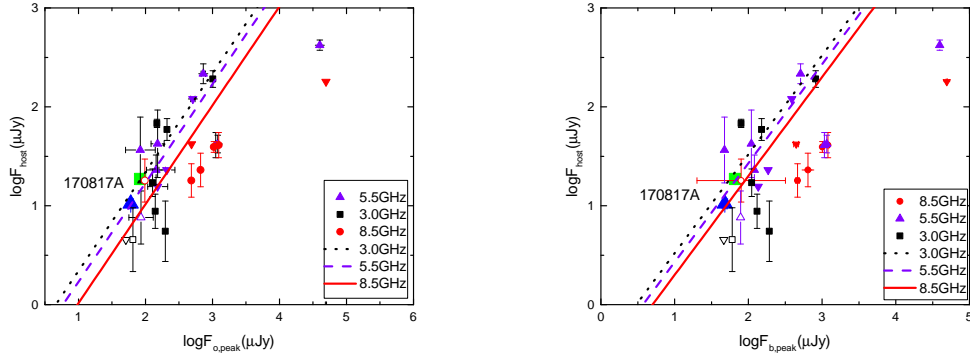


Figure 5. The relations of F_{host} versus $F_{o,peak}$ and F_{host} versus $F_{b,peak}$ are displayed on left and right panels respectively for different radio frequencies. Three correspondingly empirical power-law relations at frequencies of $\nu=8.5\text{GHz}$ (solid line), 5.5GHz (dashed line) and 3.0GHz (dotted line) are compared. Those upper limits are marked with different downward arrows. The radio-loud and the radio-quiet bursts are denoted with filled and empty symbols, individually. The off-axis GRB 170817A is symbolized with large triangle for $\nu = 5\text{GHz}$ and large square for $\nu = 3\text{GHz}$.

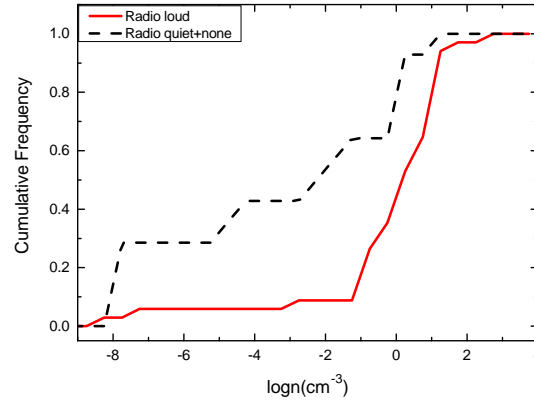


Figure 6. Cumulative fractions of $\log n$ for radio-loud (red solid line) and radio faint (black dashed line) samples.

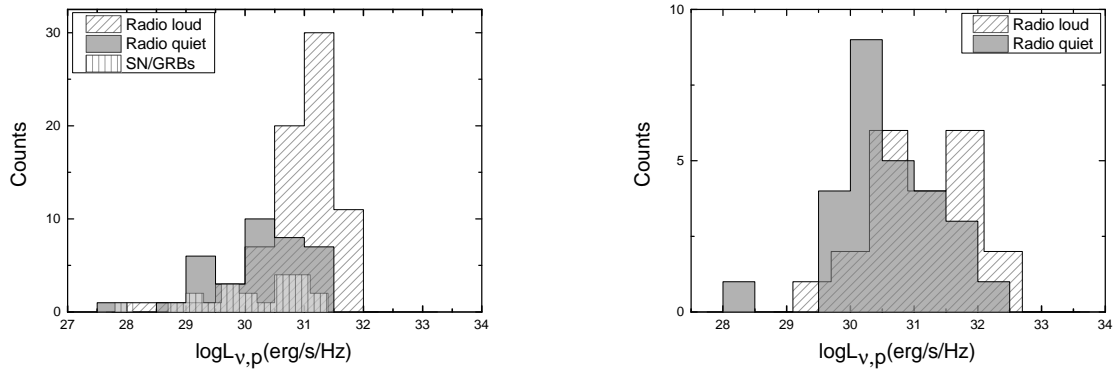


Figure 7. The left panel shows the distribution of spectral peak luminosity of the VLA-based radio afterglows. The right panel displays the distribution of spectral peak luminosity of the AMI GRBs. The filled and hatched histograms respectively represent the upper limit and detection samples, and the vertical-line hatched histogram corresponds to the SN/GRBs.

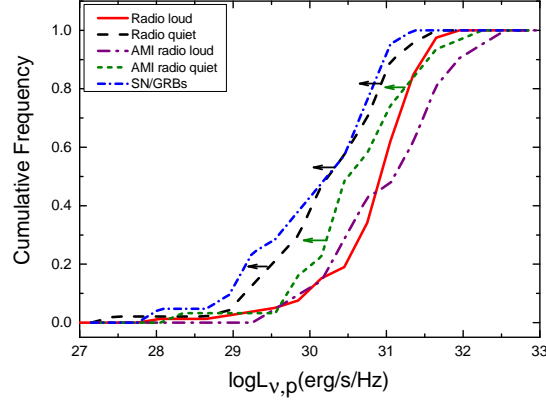


Figure 8. Cumulative fractions of $L_{v,p}$ for the VLA-based radio-loud (red solid line) and radio-quiet (black dashed line) samples, the AMI radio-loud (purple dash-dotted line), the AMI radio-quiet (green dotted line) and the SN-associated GRBs (blue short dash-dotted line). Note that the arrows denote that the $L_{v,p}$ distributions of radio-quiet GRBs are just the upper limits.

3.6 The $L_{v,p}$ - $E_{\gamma,iso}$ relationship

As shown in Figures 2, 3, 7 and 8, the averaged energies of $E_{\gamma,iso}$ and $L_{v,p}$ of radio-loud bursts are larger than the corresponding values of radio-quiet ones. In the section, we will testify the possible correlation between the $E_{\gamma,iso}$ and the $L_{v,p}$ of radio-loud (N=100) and radio-quiet (N=76) GRB samples. For this purpose, the radio peak flux densities at 8.5 GHz and 15.7 GHz have been utilized. Figure 9 displays the relations of $E_{\gamma,iso}$ with $L_{v,p}$ for all the radio-loud/quiet VLA-based bursts including 95 long GRBs (IGRBs), 23 SN/GRBs, 2 X-Ray Flashes (XRFs) and 6 short GRBs (sGRBs), and 50 AMI GRBs. Interestingly, we find on the left panel that $E_{\gamma,iso}$ is positively correlated with $L_{v,p}$ with a Pearson correlation coefficient of $R = 0.76$ ($SL = 2.2 \times 10^{-16}$) or Spearman rank correlation coefficient of 0.55 ($SL = 1.08 \times 10^{-7}$). The correlation function can be roughly written as $L_{v,p} \propto E_{\gamma,iso}^{0.41 \pm 0.04}$ for the whole radio-loud sample with $\chi^2_{\nu} = 0.23$. On the right panel, a positive correlation, $L_{v,p} \propto E_{\gamma,iso}^{0.48 \pm 0.09}$ with a $\chi^2_{\nu} = 0.42$, weakly exists for the radio-quiet bursts, of which the Pearson and the Spearman correlation coefficients are respectively $R = 0.62$ ($SL = 5.48 \times 10^{-6}$) and $R = 0.47$ ($SL = 1.2 \times 10^{-3}$) that are very close to those of the radio-loud bursts. This demonstrates that the radio peak luminosities and the prompt γ -ray energies are highly associated. It is notable that our finding here is different from Chandra et al. (2012), where they claimed no obvious correlation between $E_{\gamma,iso}$ and $L_{v,p}$ in their Figure 20 possibly owing to the limit of sample size. Recently, Tang et al. (2019) found that the X-ray peak luminosity is positively correlated with the $E_{\gamma,iso}$ as $L_X \propto E_{\gamma,iso}^{0.97}$. It is valuable to mention that the radio peak luminosities of 21 SN/GRBs in our sample and 6 SN/GRBs in Chandra et al. (2012) exhibit a consistent dependence of $E_{\gamma,iso}$. This may imply these SN/GRBs should undergo with the same processes of energy dissipations. Data points of the sGRBs and the XRFs are too limited to show if they behave a positive interdependency as the IGRBs did.

3.7 The correlation between T_{int} and $1+z$

Lloyd et al. (2019) found that there was a negative correlation between T_{int} and $1+z$ for the radio-loud rather than radio-quiet GRB sample. They concluded that if this negative correlation indeed exists, other than affected by the selection effect, it could reflect that

the systems at higher redshift have less angular momentum or less materials accreted to the GRB disks. Recently, Zhang et al. (2018) investigated the correlations between the intrinsic peak times of radio afterglows at 8.5 GHz and the redshift factor ($1+z$) and found that they are fully uncorrelated, which seems to conflict with the negative correlation of T_{int} versus $1+z$. Meanwhile, the T_{int} distribution of Swift/BAT bursts was still bimodal in that all the durations move towards to the short end once the T_{90} over $1+z$ was considered (Zhang & Choi 2008). It is well known that the sGRBs are usually observed at nearby universe unlike the IGRBs. Strictly speaking, the negative dependence of the T_{int} on the redshift is hard to understand unless a fraction of sGRBs have extremely small redshift while parts of IGRBs have very high redshift.

As mentioned in Section 2, our current samples as an expansion of Lloyd et al. (2019) are relatively complete. Therefore, it is timely and essential to check if the correlations between T_{int} and $1+z$ coexist in both radio-loud, radio-quiet and radio-none samples as plotted in Figure 10. In statistics, the Pearson correlations of T_{int} vs. $1+z$ for the radio-loud and the radio-quiet samples give the R-indexes as -0.29 ($SL=0.012$), -0.35 ($SL=0.018$) and -0.15 ($SL=0.53$) for the radio-loud, the radio-quiet and radio-none IGRB samples, respectively. This demonstrates that the radio-loud GRBs do have a weaker negative correlation of T_{int} with redshift, of which this result is in good agreement with Lloyd et al. (2019). Additionally, our radio-quiet sample also hold the similar anti-correlation with a 95.4% confidence level like the radio-loud GRBs. It is surprisingly found that there is very weak correlation between T_{int} and $1+z$ for the radio-none sample. We notice that the sGRBs in any case of our samples are outliers of the T_{int} - $(1+z)$ correlation of the IGRBs and the sGRBs with smaller T_{int} and $1+z$ are systematically located at the bottom-left side of plane. Particularly, the radio-loud sGRB 170817A is situated in the region of normal sGRBs. Hence, the T_{int} distributions of two kinds of GRBs are well in agreement with Zhang & Choi (2008).

4 CONCLUSION AND DISCUSSION

Based on the above systematic investigations of a relatively ‘‘complete’’ sample of radio-selected GRBs, we briefly summarize our main results as follows:

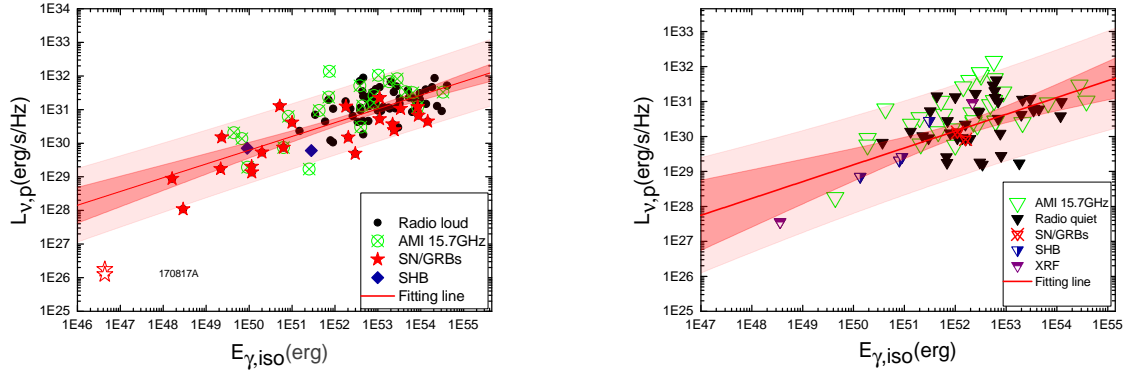


Figure 9. The correlations of $L_{\nu,p}$ versus $E_{\gamma,iso}$ for radio-loud sample (the left panel) and radio-quiet sample (the right panel). All illustrations are marked on the insert. Note that the inverted triangles stand for the upper limits. Except the AMI radio-loud (cross circles) and radio-quiet (empty triangles) GRBs, all other symbols represent the VLA-based bursts. GRB 170817A detected at $\nu = 3$ and 5.5 GHz has been marked with two empty stars. The solid lines are the best power-law fits to all bursts but GRB 170817A. The light shaded regions are 2σ confidence ranges and the heavy shaded areas show the 2σ prediction ranges.

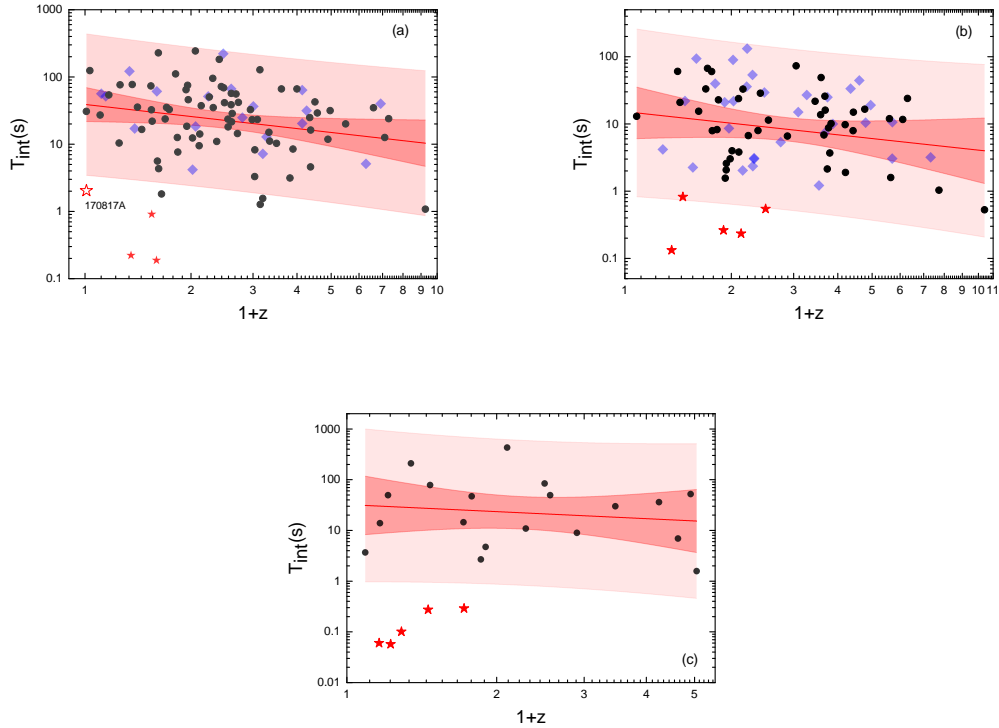


Figure 10. Panel (a), (b) and (c) respectively show the correlations between T_{int} and $1+z$ for the radio-loud, radio-quiet and radio-none samples. The filled circles and diamonds denote IGRBs and the filled stars represent sGRBs. The red solid lines are the best fits to the observed data with a confidence level of 95.4% (heavy shadow region) and a prediction of 2σ range (light shadow region). The AMI data at 15.7 GHz have been symbolized with blue diamonds. The radio-loud sGRB 170817A characterized with empty star is displayed in Panel (a).

- According to the distributions of z , T_{int} , $E_{\gamma,iso}$ and $L_{\nu,p}$, we find that the radio-loud, the radio-quiet and the radio-none samples observationally differ with each other, particularly for the two energies $E_{\gamma,iso}$ and $L_{\nu,p}$. The radio-loud sample is not required to be redivided into two subgroups.

- It is also supported that the radio-loud and the radio-faint (radio-quiet plus radio-none) GRBs have largely different distribu-

tions of the radio isotropic energies and the surrounding medium densities, and could be thus originated from diverse central engines.

- Although the radio flux density distributions of host galaxies for the radio-loud and the radio-faint samples are not significantly different, the flux densities of the radio-quiet GRBs and their host galaxies are relatively lower than those of the radio-loud ones, which

indicates the host types of the radio-loud and the radio-faint GRBs might be diverse in essence.

- The mean values of z , $F_{o,peak}$, T_{int} , $E_{\gamma,iso}$, n and $L_{\nu,p}$ for the radio-faint GRBs are comparatively smaller than those of the radio-loud sample correspondingly. Especially, it can be seen from Figures 3, 10 and A1 that the radio-quiet GRBs with the lowest means of z and T_{int} are unique and different from other radio-selected bursts.

- Interestingly, we find $E_{\gamma,iso}$ and $L_{\nu,p}$ are correlated with the power law relations of $L_{\nu,p} \propto E_{\gamma,iso}^{0.41}$ for the radio-loud sample and $L_{\nu,p} \propto E_{\gamma,iso}^{0.48}$ for the radio-quiet sample, which were not distinguished by Chandra et al. (2012) for the correlation between $E_{\gamma,iso}$ and the peak radio spectral luminosity.

- We follow Lloyd et al. (2019) to study the dependencies of T_{int} with z for different radio-selected samples. Excitingly, we not only gain the anti-correlation between T_{int} and z for the radio-loud sample as Lloyd et al. (2019) proposed, but also find that this dependency holds for the radio-quiet instead of the radio-quiet sample.

- Despite of the AMI radio afterglows detected at higher frequency, all the above conclusions based on the VLA-based GRB samples are well supported.

Most of our radio-selected GRBs are IGRBs that are thought to be produced from core collapse of massive stars to form a black hole (Woosley 1993, MacFadyen & Woosley 1999). In the collapsar model, the intrinsic time T_{int} relies on the accretion rate that is related with the momentum of the progenitor system, namely larger momentum corresponds to longer T_{int} , and the masses forming the accretion disk (Janiuk & Proga 2008). The collapsing progress exists in either a single stellar system or a binary system with three scenarios (Fryer et al. 1999), i.e. Scenario I: a single star evolves off main sequence and its winds blow off the hydrogen envelope to form a helium core, and then this helium core collapses to produce the GRBs; Scenario II: a binary system with primary evolving off main sequence evolves into a common envelope phase, and then after the H envelope was ejected the primary becomes a helium core collapsing and accreting the secondary to produce GRBs; Scenario III: this is also a binary system with primary evolving off main sequence into a common system, and then the secondary evolving off main sequence too, subsequently the system enters into a double-helium-star binary system. Finally, the two helium stars merge into one helium star and then the helium core collapses to cause the GRBs (Fryer et al. 1999). Because T_{int} is tightly determined by the momentum of collapsing systems, together with more masses accreted on the disk, Scenario I would readily lead to the longer T_{int} even though its angular momentum is expected to be less than the other two Scenarios (Fryer & Woosley 1998, Zhang & Fryer 2001).

Note that the soft IGRBs associated with core-collapse supernovae (Galama et al. 1998; Woosley et al. 1999; Fryer et al. 1999; Stanek et al. 2003; Hjorth et al. 2003; Campana et al. 2006; Xu et al. 2013) are generally believed to result from the deaths of massive stars. However, the hard sGRBs are usually thought to occur owing to the coalescence of two compact stars, such as double neutron stars, or a neutron star plus black hole system (Lee et al. 2007; Berger et al. 2014). Therefore, the sGRBs with lower redshifts and isotropic γ -ray energies would be expected to have relatively shorter T_{int} in comparison with the IGRBs. We investigate the association of $E_{\gamma,iso}$ with T_{int} in Figure 11, from which we can see that there are no any correlations for either the sGRBs or the IGRBs. However, they can be separated by a horizontal line of $T_{int} = 1$ s and a vertical line of $E_{\gamma,iso} = 4 \times 10^{51}$ erg. All sGRBs but GRB 170817A possessing smaller $E_{\gamma,iso}$ and T_{int} are located at the bottom-left corner. In comparison, the IGRBs with longer T_{int} relatively generate

larger $E_{\gamma,iso}$ spanning from $\sim 10^{48}$ erg to $\sim 10^{55}$ erg. Even though some IGRBs and sGRBs have comparable $E_{\gamma,iso}$, their T_{int} values are completely distinct. It is valuable to focus on GRB 090429B, lying at the bottom-right corner, that is the farthest burst detected so far with $z \approx 9.4$ and $T_{90} = 5.5$ s (Cucchiara et al. 2011), whose progenitor is expected to be different from other lower redshift, especially short GRBs. Furthermore, we caution that sGRB 170817A differs from both the normal sGRBs and the low energy IGRBs as depicted in Figure 11. Very recently, Tang et al. (2019) found that the $E_{\gamma,iso}$ and the T_{90} are positively correlated, and they explained that this might happen when the observed intensities of γ -rays were constrained within a certain range. We nevertheless find that the positive correlation trend disappears for the IGRBs in the co-moving frame. In principal, one may pursue to convert the observed $E_{\gamma,iso}$ into the co-moving quantity by use of $E'_{\gamma,iso} \simeq E_{\gamma,iso}/\Gamma$, where Γ is the bulk Lorentz factor (Ghirlanda et al. 2012). Unfortunately, the Lorentz factor is still very hard to be determined precisely and uniquely although many authors have made great efforts (e.g., Sari & Piran 1999; Pe'er 2007; Liang et al. 2010; Zou et al. 2010, 2015; Ghirlanda et al. 2018), which will be confirmed by further observations of the next-generation telescopes.

5 ACKNOWLEDGE

This work is supported by the Research Foundation of China (grant Nos. ZR2018MA030, XKJJC201901 and 201909118), the National Natural Science Foundation of China (grant No. U1938201, 11873030, 11673023, U1838201, U1838202 and U1838104), the Strategic Priority Research Program of the Chinese Academy of Sciences ("Multiwaveband Gravitational Wave Universe", grant No. XDB23040000; Grant No. XDA15360300) and the National Key R&D Program of China (2016YFA0400800). We thank Poonam Chandra for kindly offering the data of GRB radio afterglows observed by VLA. We also acknowledge E. W. Liang, L. B. Li and H. Y. Chang for helpful discussions.

REFERENCES

- Abbott B. P., Abbott R., Abbott T. D., et al., 2017, *ApJ*, **848**, L13
 Alexander K. D., Berger E., Fong W., et al., 2017, *ApJ*, **848**, L21
 Anderson G. E., Staley T.D., van der Horst A.J., et al., 2018, *MNRAS*, **473**, 1512
 Becerra R. L., Watson A.M., Fraija N., et al., 2019, *ApJ*, **872**, 118
 Berger E., 2014, *ARA&A*, **52**, 43
 Berger E., Kulkarni S.R., Pooley G., et al., 2003, *Nature*, **426**, 154
 Berger E., Price P.A., Cenko S.B., et al., 2005, *Nature*, **438**, 988
 Bloom J.S., Frail D.A., Blustin A. J., Kulkarni S.R., 2003, *ApJ*, **594**, 674
 Campana S., Mangano V., Blustin A. J., et al., 2006, *Nature*, **442**, 1008
 Cenko S.B., Kasliwal M., Harrison F.A., et al., 2006, *ApJ*, **652**, 490
 Cenko S.B., Frail D.A., Harrison F.A., et al., 2011, *ApJ*, **732**, 29
 Chandra P., Cenko S.B., Frail D. A et al., 2008, *ApJ*, **683**, 924
 Chandra P., Frail D. A., Fox D., et al., 2010, *ApJ*, **712**, L31
 Chandra P., Frail D. A., 2012, *ApJ*, **746**, 156
 Cucchiara G., Mangano V., Chincarini G., et al., 2007, *A&A*, **462**, 73
 Cucchiara A., Levan A. J., Fox D. B., et al., 2011, *ApJ*, **736**, 7
 Duncan R. C., Thompson C., 1992, *ApJ*, **392**, L9
 Fong W., Berger E., Margutti R., Zauderer B. A., 2015, *ApJ*, **815**, 102
 Frail, D. A., Waxman, E., Kulkarni, S. R. 2000, *ApJ*, **537**, 191
 Frail, D. A., Yost S.A., Berger E., et al. 2003, *ApJ*, **590**, 992
 Frail, D. A., Cameron P.B., Kasliwal M., et al. 2006, *ApJ*, **646**, L99
 Friedman A. S., Bloom J. S., 2005, *ApJ*, **627**, 1
 Fryer C. L., Woosley S. E., 1998, *ApJ*, **502**, L9
 Fryer C. L., Woosley S. E., Hartmann D. H., 1999, *ApJ*, **526**, 152

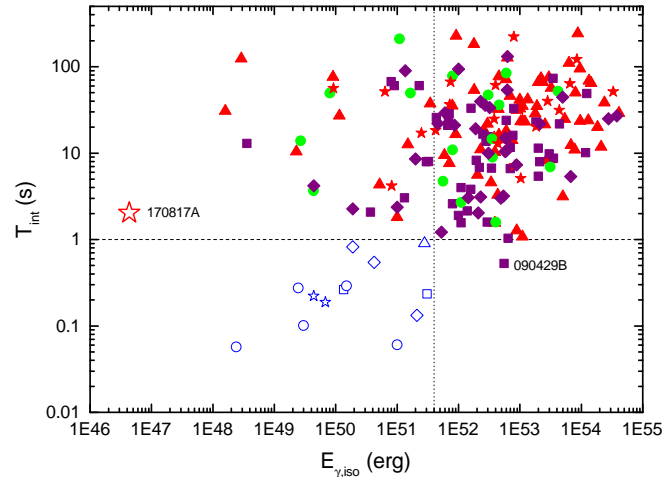


Figure 11. Relations of T_{int} with $E_{\gamma,iso}$ for the radio-loud (triangles), radio-quiet (squares) and radio-none (circles) IGRB (filled symbols) and sGRB (empty symbols) in the VLA-based samples. Vertical and horizontal lines stand for $E_{\gamma,iso} = 4 \times 10^{51}$ erg and $T_{int} = 1$ s, correspondingly. The radio-loud and radio-quiet bursts in the AMI samples are identified with small stars and diamonds, respectively. sGRB 170817A is marked with a large star.

- Geng J. J., Dai Z., G., Huang Y. F. et al., 2018, *ApJ*, **856**, L33
 Ghisellini G., Nardini M., Ghirlanda G., Celotti A., 2009, *MNRAS*, **393**, 253
 Galama T. J., Vreeswijk P. M., van Paradijs J., et al. 1998, *Nature*, **395**, 670
 Ghirlanda G., Nava L., Ghisellini G., et al. 2012, *MNRAS*, **420**, 483
 Ghirlanda G., Nappo F., Ghisellini G., et al. 2018, *A&A*, **609**, 112
 Goldstein A., Veres P., Burns E., et al., 2017, *ApJ* **848**, L14
 Hancock P. J., Geansler B. M., Murphy T., 2013, *ApJ*, **776**, 106
 Hascoët R., Beloborodov A. M., Daigne F., Mochkovitch R., 2017, *MNRAS*, **472**, L94
 Hjorth J., Sollerman J., Møller, P., et al. 2003, *Nature*, **423**, 847
 Huang Y. F., Dai Z. G., Lu T., 1999, *A&A* **309**, 513
 Huang Y. F., Gou L. J., Dai Z. G., Lu T., 2003, *ApJ* **543**, 90
 Janiak A., Proga D., 2008, *ApJ*, **675**, 519
 Klebesadel R. W., Strong I. B., Olson R. A., 1973, *ApJ*, **182**, L85
 Kouveliotou C., Meegan C.A., Eishman G.J., et al, 1993, *ApJ*, **413**, 101
 Laskar T., Alexander K.D., Berger E., et al., 2018, *ApJ*, **862**, 94
 Laskar T., Hull C.L.H., Cortes P., et al., 2020, *ApJ*, **895**, 64
 Lee William H., Ramirez-Ruiz Enrico, 2007, *New Journal of Physics*, **9**, 17
 Li L. B., Zhang Z. B., Huang Y. F., et al, 2015, *MNRAS*, **451**, 1815
 Li L. B., Geng J. J., Huang Y. F., et al, 2018, *ApJ*, **880**, 39
 Liang E. W., Yi S. X., Zhang J., et al, 2010, *ApJ*, **725**, 2209
 Lloyd-Ronning N. M., Fryer C. L., 2017, *MNRAS*, **467**, 3413
 Lloyd-Ronning N. M., Gompertz B., Pe'er A., et al., 2019, *ApJ*, **871**, 118
 MacFadyen A. I., Woosley S. E., 1999, *ApJ*, **524**, 262
 Mészáros P., 2006, *RPPH* **69**, 2259
 Mu H. J., Lin D.B., Xi S.Q., et al. 2016, *ApJ*, **831**, 111
 Paczynski B., 1990, *ApJ*, **363**, 218
 Panaitescu A., Kumar P., 2002, *ApJ*, **571**, 779
 Pe'er A., Ryde F., Wijers Ralph A. M. J., et al., 2007, *ApJ*, **664**, L1
 Piran T., 1999, *PhR*, **314**, 575
 Rees M. J., Meszaros P., 1992, *MNRAS*, **258**, 41
 Rees M. J., Meszaros P., 1994, *ApJ*, **430**, L93
 Rhodes L. et al., van der Horst A.J., Fender R., et al., 2020, *MNRAS*, **496**, 3326
 Sari R., Piran T., 1999, *ApJ*, **517**, L109
 Schaefer B. E., 2007, *ApJ*, **660**, 16
 Schaefer B. E., Brandley E., Gerardy C.L., et al. 2003, *ApJ*, **588**, 387
 Savchenko V., Ferrigno C., Kuulkers E., et al., 2017, *ApJ*, **848**, L15
 Soderberg A. M., Kulkarni S.R., Berger E., et al. 2004, *Nature*, **430**, 648
 Soderberg A. M., Berger E., Kasliwal M., et al, 2006a, *ApJ*, **650**, 261
 Soderberg A. M., Kulkarni S.R., Nakar E., et al, 2006b, *Nature*, **442**, 1014
 Stanek K. Z., Matheson T., Garnavich P. M., et al, 2003, *ApJ*, **591**, L17
 Tang C. H., Huang Y. F., Geng J. J., Zhang Z. B., et al., 2019, *ApJS*, **245**, 1
 Tashiro M. S., Abe K., Angelini L., et al., 2007, *PASJ*, **59**, S361
 de Ugarte Postigo A., Fatkhullin T.A., Johannesson G., et al., 2007, *A&A*, **462**, L57
 Urata Y. J., Toma K., Huang K. Y., et al., 2019, *ApJ*, **884**, L58
 Wijers R. A. M. J., Galama T. J., 1999, *ApJ*, **523**, 177
 Woosley S. E., 1993, *ApJ*, **405**, 273
 Woosley S. E., MacFadyen A. I., 1999, *A&AS*, **138**, 499
 Xu D., de Ugarte Postigo A., Leloudas G., et al, 2013, *ApJ*, **776**, 98
 Zhang Z. B., Choi C. S., 2008, *A&A*, **484**, 293
 Zhang Z. B., Chandra P., Huang Y. F., & Li D., 2018, *ApJ*, **865**, 82
 Zhang W., Fryer C. L., 2001, *ApJ*, **550**, 357
 Zhang B., 2014, *IJMPD*, **23**, 2
 Zou Y. C., Piran T., 2010, *MNRAS*, **402**, 1854
 Zou Y. C., Cheng K. S., Wang F.Y., 2015, *ApJ*, **800**, 23

Table 1: Physical parameters of radio-loud GRBs

GRB	T_{90} (s)	z	$E_{\gamma,iso}$ (erg)	n (cm^{-3})	$L_{\nu,p}$ (erg/s/Hz)	$f_{p,radio}$ (uJy)	RMS (uJy)	Radio Telescope	reference
970508	14	0.835	7.10E+51	1	9.40E+30	1270	33	VLA	1,4
970828	147	0.958	2.96E+53	...	2.93E+30	147	33	VLA	1
980329	58	2-3.9	2.10E+54	20^{+10}_{-10}	4.76E+31	465	16	VLA	1,5
980425*	31	0.009	1.60E+48	...	8.56E+28	49400	1000	ATCA	1
980519	30	$0.14^{+0.32}_{-0.03}$	1.95E+31	1050	20	VLA	1,5
980703	90	0.966	6.90E+52	28^{+10}_{-10}	1.95E+31	1050	55	VLA	1,6
981226	20	1.11	5.90E+51	...	4.40E+30	169	28	VLA	1
990123	100	1.6	2.39E+54	...	1.28E+31	260	32	VLA	1
990506	220	1.307	9.49E+53	...	2.02E+31	581	45	VLA	1
990510	75	1.619	1.78E+53	$0.29^{+0.11}_{-0.15}$	1.14E+31	127	30	ATCA	1,7
991208*	60	0.706	1.10E+53	18^{+18}_{-6}	2.23E+31	1990	33	VLA	1,7
991216	25	1.02	6.75E+53	$4.7^{+6.8}_{-1.8}$	2.14E+31	960	67	VLA	1,7
000131	110	4.5	1.84E+54	...	4.64E+31	207	46	ATCA	1
000210	10	0.85	2.00E+53	...	1.48E+30	93	21	VLA	1
000301C	10	2.034	4.37E+52	27^{+5}_{-5}	2.29E+31	483	41	VLA	1
000418	30	1.119	7.51E+52	27^{+250}_{-14}	2.26E+31	1240	33	VLA	1,7
000911*	500	1.059	8.80E+53	...	6.65E+30	278	36	VLA	1
000926	25	2.039	2.70E+53	27^{+3}_{-3}	4.84E+31	666	60	VLA	1,7
001007	375	222	33	VLA	1
001018	31	405	50	VLA	1
010222	170	1.477	1.33E+54	1.7	1.48E+31	344	39	VLA	1,7
010921	24	0.45	9.00E+51	...	1.06E+30	229	22	VLA	1
011030	...	<3	2.26E+31	219	20	VLA	1
011121	105	0.362	4.55E+52	...	1.83E+30	610	39	ATCA	1
011211	400	2.14	6.30E+52	...	1.18E+31	163	17	VLA	1
020305	247	76	15	VLA	1
020405*	40	0.69	1.10E+53	8	5.22E+30	487	34	VLA	1,5
020813	113	1.254	8.00E+53	...	1.04E+31	323	39	VLA	1
020819B	50	0.41	7.90E+51	...	1.22E+30	315	18	VLA	1
020903*	13	0.25	2.30E+49	...	1.51E+30	1058	19	VLA	1
021004	50	2.33	3.80E+52	30^{+270}_{-27}	5.35E+31	691	33	VLA	1,8
021206	20	1377	47	VLA	1
030115	36	2.5	3.91E+52	...	9.34E+30	94	22	VLA	1
030226	69	1.986	1.20E+53	...	9.14E+30	131	27	VLA	1
030323	20	3.372	3.39E+52	...	4.28E+30	530	170	VLA	1
030329*	63	0.169	1.80E+52	1.8	1.01E+31	19150	80	VLA	1,9
030723	31	219	22	VLA	1
031203*	30	0.105	1.15E+50	0.6	1.34E+29	811	40	VLA	1,10
040812	19	450	80	VLA	1
041219A	6	518	150	VLA	1
050315	96	1.95	5.70E+52	...	2.03E+31	300	62	VLA	1
050401	33	2.898	3.20E+53	10	1.51E+31	122	33	VLA	1,3
050416A*	3	0.65	1.00E+51	3	4.12E+30	431	46	VLA	1,3
050509C	25	404	58	VLA	1
050525A*	9	0.606	2.04E+52	1.0×10^{-8}	1.37E+30	178	46	VLA	1,3
050603	12	2.821	5.00E+53	...	3.11E+31	316	45	VLA	1
050713B	125	426	45	VLA	1
050724	96	0.258	9.00E+49	0.1	7.08E+29	465	29	VLA	1,11
050730	157	3.968	9.00E+52	8	4.04E+31	212	35	VLA	1,3
050820A	240	2.615	2.00E+53	0.1	6.74E+31	634	62	VLA	1,12
050824	23	0.83	1.50E+51	1	2.32E+30	152	34	VLA	1,3
050904	174	6.29	1.30E+54	680	3.01E+31	116	18	VLA	1,13
050922C	5	2.199	3.90E+52	2	1.15E+31	140	42	VLA	1,3
051022	200	0.809	6.30E+53	...	8.49E+30	585	49	VLA	1
051109A	37	2.346	2.30E+52	...	1.06E+31	117	24	VLA	1
051111	46	1.55	6.00E+52	5.00×10^{-9}	4.56E+30	98	28	VLA	1,3
051211B	80	68	19	VLA	1
051221A	1.4	0.547	2.80E+51	0.001	6.01E+29	88	26	VLA	1,14

Table 1: Physical parameters of radio-loud GRBs

GRB	T_{90} (s)	z	$E_{\gamma,iso}$ (erg)	n (cm^{-3})	$L_{\nu,p}$ (erg/s/Hz)	$f_{p,radio}$ (μ Jy)	RMS (μ Jy)	Radio Telescope	reference
060116	106	363	28	VLA	1
060218*	128	0.033	2.90E+48	5	1.09E+28	453	77	VLA	1,15
060418	103	1.49	1.00E+53	10	9.41E+30	216	48	VLA	1,3
061121	81	1.315	1.90E+53	3	1.07E+31	304	48	VLA	1,3
061222A	72	2.088	1.03E+53	...	2.15E+31	285	68	VLA	1
070125	60	1.548	9.55E+53	42	2.61E+31	660	39	VLA	1,16
070612A	369	0.617	9.12E+51	...	5.09E+30	589	54	VLA	1
071003	148	1.604	3.24E+53	...	2.12E+31	431	51	VLA	1
071010B	36	0.947	2.60E+52	...	6.43E+30	330	52	VLA	1
071020	4	2.146	8.91E+52	...	1.47E+31	186	22	VLA	1
071021	229	<5.6	4.39E+31	149	44	VLA	1
071109	30	188	42	VLA	1
071122	80	1.14	3.47E+51	...	6.96E+30	255	45	VLA	1
080229	64	635	44	VLA	1
080319B*	125	0.937	1.45E+54	10	4.43E+30	232	42	VLA	1,3
080603A	150	1.687	1.23E+31	230	29	VLA	1
080810	108	3.35	5.37E+53	...	2.29E+31	151	50	VLA	1
081203B	23	162	44	VLA	1
081221	34	167	27	VLA	1
090313	71	3.375	4.57E+52	0.6	8.81E+31	576	44	VLA	1
090323	133	3.57	4.10E+54	0.1	3.72E+31	225	35	VLA	1,17
090328	57	0.736	1.00E+53	0.26	9.81E+30	809	39	VLA	1,17
090418	56	1.608	2.57E+53	...	1.08E+31	219	44	VLA	1
090423	10	8.26	1.10E+53	0.9	4.63E+31	92.4	22.7	VLA	1,18
090424	50	0.544	4.47E+52	...	4.54E+30	673	39	VLA	1
090618*	113	0.54	2.21E+53	...	3.67E+30	551	51	VLA	1
090709A	89	<6.1	5.68E+31	174	53	VLA	1
090715B	265	3	2.36E+53	...	3.33E+31	257	57	VLA	1
090902B	...	1.883	3.09E+54	...	8.33E+30	130	34	VLA	1
091020	39	1.71	4.56E+52	...	2.47E+31	451	44	VLA	1
100413A	191	<3.5	2.56E+31	159	15	EVLA	1
100414A	26	1.368	7.79E+53	...	1.56E+31	415	15	EVLA	1
100418A*	7	0.62	5.20E+50	...	3.99E+30	458	22	EVLA	1
100805A	15	108	32	EVLA	1
100814A	175	1.44	5.97E+52	...	1.90E+31	462	25	EVLA	1
100901A	439	1.408	1.78E+52	...	1.74E+31	440	27	EVLA	1
100906A	114	1.727	1.34E+53	...	1.20E+31	215	28	EVLA	1
101219B*	34	0.552	2.96E+52	...	4.93E+29	71	15	EVLA	1
110428A	5.6	69	18	EVLA	1
120320A	25.74	380	80	AMI	19,20
120326A	69.6	1.798	3.82E+52	...	5.12E+31	860	80	AMI	19,20
120514A	164.4	460	130	AMI	19,20
121031A	62.5	0.1126	1.91E+29	670	220	AMI	19,20
121128A	23	2.2	8.20E+52	...	2.62E+31	320	90	AMI	19,20
130216A	6.5	990	100	AMI	19,20
130427A*	162.83	0.338	8.50E+53	...	1.19E+31	4540	80	AMI	19,20
130419A	75.7	1700	120	AMI	19,20
130508A	42	550	140	AMI	19,20
130603A	470	130	AMI	19,20
130604A	37.7	1.06	9.34E+30	390	70	AMI	19,20
130606A	276.58	5.91	2.83E+53	...	8.17E+31	260	70	AMI	19,20
130608A	44.4	240	80	AMI	19,20
130612A	110	2.006	7.19E+51	...	2.34E+31	330	90	AMI	19,20
130625A	38.1	590	110	AMI	19,20
130702A*	59	0.145	6.36E+50	...	7.42E+29	1560	130	AMI	19,20
130907A	115	1.238	3.30E+54	...	3.29E+31	1040	100	AMI	19,20
131024B	64	610	70	AMI	19,20
140108A	97.8	0.6	4.00E+52	...	3.03E+30	370	50	AMI	19,20

Table 1: Physical parameters of radio-loud GRBs

GRB	T_{90} (s)	z	$E_{\gamma,iso}$ (erg)	n (cm^{-3})	$L_{\nu,p}$ (erg/s/Hz)	$f_{p,radio}$ (μJy)	RMS (μJy)	Radio Telescope	reference
140209A	21.3	430	90	AMI	19,20
140215A	84.2	240	50	AMI	19,20
140304A	32	5.28	1.03E+53	...	1.04E+32	380	40	AMI	19,20
140305A	13.7	420	40	AMI	19,20
140318A	8.43	1.02	6.25E+30	280	40	AMI	19,20
140320B	470	30	AMI	19,20
140320C	140	40	AMI	19,20
140423A	134	3.26	4.38E+53	...	3.35E+31	230	70	AMI	19,20
140430A	173.6	1.6	1.37E+32	2800	110	AMI	19,20
140606A	0.34	530	50	AMI	19,20
140606B	23.6	0.384	2.50E+51	...	1.69E+29	50	60	AMI	19,20
140607A	109.9	590	80	AMI	19,20
140629A	42	2.275	4.40E+52	...	1.29E+31	150	50	AMI	19,20
140703A	84	3.14	1.84E+53	...	6.78E+31	490	60	AMI	19,20
140709A	98.6	460	40	AMI	19,20
140713A	5.3	1370	40	AMI	19,20
140903A	0.3	0.351	4.40E+49	...	2.04E+30	720	70	AMI	19,20
141015A	11	280	60	AMI	19,20
141020A	15.55	300	60	AMI	19,20
141109B	54.2	910	250	AMI	19,20
141121A	549	1.47	8.00E+52	...	1.57E+31	370	40	AMI	19,20
141212A	0.3	0.596	6.80E+49	...	1.37E+30	170	40	AMI	19,20
141212B	10.5	110	30	AMI	19,20
150110B	10.6	530	40	AMI	19,20
150413A	263.6	3.139	6.53E+53	...	3.18E+31	230	40	AMI	19,20
150213B	181	140	40	AMI	19,20
161219B*	6.94	0.1475	1.16E+50	...	1.37E+29	278.1	28.6	VLA	19,21
171205A*	189.4	0.0368	2.18E+49	...	1.71E+29	5710	50	VLA	19,22
180720B*	49	0.654	3.40E+53	...	1.06E+31	1096	62	AMI	19,23
190114C*	361.5	0.42	2.40E+53	...	2.46E+30	607	17.3	VLA	19,23
190829A*	58.2	0.0785	2.00E+50	...	5.36E+29	3889	197	AMI	19,24

Note. In Column 1, \star presents the SN/GRB. References are given in order for duration time (T_{90}), redshift(z), isotropic equivalent energy($E_{\gamma,iso}$), peak flux density($f_{p,radio}$) and medium density(n), respectively. [1]Chandra et al. (2012); [2]Friedman & Bloom (2005); [3]Ghisellini et al. (2009); [4]Frail et al. (2000); [5]Bloom et al. (2003); [6]Frail et al. (2003); [7]Panaitescu et al. (2002); [8]Schaefer et al. (2003); [9]Berger et al. (2003); [10]Soderberg et al. (2004); [11]Berger et al. (2005); [12]Cenko et al. (2006); [13]Frail et al. (2006); [14]Soderberg et al. (2006a); [15]Soderberg et al. (2006b); [16]Chandra et al. (2008); [17]Cenko et al. (2011); [18]Chandra et al. (2010); [19]https://gcn.gsfc.nasa.gov/gcn3_archive.html; [20]Anderson et al. (2018); [21]Laskar et al. (2018); [22]Urata et al (2019); [23]Rhodes (et al.); [24]Laskar et al. (2020).

Table 2: Physical parameters of radio-quiet GRBs

GRB	T_{90} (s)	z	$E_{\gamma,iso}$ (erg)	n (cm^{-3})	$L_{\nu,p}$ (erg/s/Hz)	$f_{p,radio}$ (μJy)	RMS (μJy)	Radio Telescope	reference
970228*	56	0.695	1.60E+52	...	8.26E+29	76	50	VLA	1
971214	35	3.42	2.11E+53	...	1.14E+31	73	50	VLA	1
980613	50	1.097	6.90E+51	...	1.78E+29	7	28	VLA	1
990705	42	0.84	1.82E+53	...	1.71E+29	11	36	ATCA	1
990712	30	0.433	6.72E+51	...	2.58E+29	60	50	ATCA	1
000630	20	70	62	VLA	1
020124	41	3.2	3.00E+53	3	1.19E+31	84	30	VLA	1,7
020305	247	<2.8	76	15	VLA	1
020410	1800	64	51	ATCA	1
021211*	8	1.01	1.10E+52	...	1.32E+30	60	28	VLA	1
030131	124	8	35	VLA	1
030227	33	64	24	VLA	1
030418	110	69	27	VLA	1
030429	25	2.658	2.19E+52	...	9.14E+30	84	54	VLA	1
040106	47	5	50	VLA	1
050215B	8	59	181	VLA	1
050306	158	56	28	VLA	1
050408	15	1.236	3.44E+52	0.01	1.58E+29	5	39	VLA	1,6
050607	26	59	23	VLA	1
050713A	120	3	...	17	58	VLA	1,3
050801	19	1.38	3.24E+51	1.00×10^{-8}	5.31E+30	139	50	VLA	1,5
050814	151	5.3	6.00E+52	...	2.01E+31	73	36	VLA	1
050815	3	77	45	VLA	1
050915A	52	43	31	VLA	1
051016B	4	0.936	3.70E+50	...	6.67E+29	35	13	VLA	1
051021A	27	36	25	VLA	1
051109B	14	0.08	3.60E+48	...	3.58E+27	25	23	VLA	1
051227	115	0.714	8.00E+50	...	2.06E+29	18	25	VLA	1
060105	54	3	...	49	47	VLA	1,4
060108	14	<2.8	12	25	VLA	1
060124	<59	31	VLA	1
060522	71	5.11	7.00E+52	...	1.00E+31	38	17	VLA	1
060604	95	2.68	4.37E+51	...	1.43E+31	130	65	VLA	1
060605	79	3.773	2.50E+52	...	1.67E+31	94	47	VLA	1
060707	66	3.43	6.10E+52	...	1.28E+31	82	41	VLA	1
060719	67	<4.6	4.15E+31	180	60	ATCA	1
060801	0.5	1.131	3.09E+51	...	2.83E+30	105	35	VLA	1
060825	8	94	47	VLA	1
060908	19	1.884	7.00E+52	10	3.27E+30	51	26	VLA	1,5
060912A	5	0.937	8.00E+51	...	1.24E+30	65	32	VLA	1
060923A	52	110	55	VLA	1
060923C	76	100	50	VLA	1
060926	8	3.209	1.00E+52	...	1.34E+31	94	56	VLA	1
061028	106	0.76	2.29E+51	...	1.03E+30	80	40	VLA	1
061126	71	1.159	8.00E+52	1.00×10^{-8}	2.81E+29	10	36	VLA	1,5
061210	85	0.41	9.00E+50	...	2.62E+29	68	34	VLA	1
070220	129	15	50	VLA	1
070223	89	<11	47	VLA	1
070311	50	21	51	VLA	1
070429B	0.5	0.902	1.35E+50	...	7.12E+28	4	100	VLA	1
070610	10	80	100	VLA	1
070714B	3	0.923	1.10E+52	$0.056^{+0.024}_{-0.011}$	1.67E+30	<48	45	VLA	1,2
070724B	50	<47	36	VLA	1
070729	0.9	<99	85	VLA	1
071010A	6	0.985	1.32E+51	3	1.47E+30	<66	35	VLA	1,5
071011	81	<106	60	VLA	1
071018	288	<3	39	VLA	1
071112C	15	0.823	1.95E+52	...	1.14E+30	<57	38	VLA	1
080212	117	83	51	VLA	1
080413B	8	1.101	1.59E+52	...	2.21E+30	86	36	VLA	1
080430	14	0.767	3.00E+51	...	8.92E+29	68	46	VLA	1
080503	0.3	3	30	VLA	1
080506	152	<40	40	VLA	1
080507	30	44	49	VLA	1

Table 2: Physical parameters of radio-quiet GRBs

GRB	T_{90} (s)	z	$E_{\gamma,iso}$ (erg)	n (cm^{-3})	$L_{\nu,p}$ (erg/s/Hz)	$f_{p,radio}$ (μJy)	RMS (μJy)	Radio Telescope	reference
080603B	59	2.689	7.70E+52	...	1.22E+30	11	41	VLA	1
080604	69	1.417	7.08E+51	...	3.12E+30	<70	39	VLA	1
080613A	30	7	46	VLA	1
080702A	0.5	<82	52	VLA	1
080721	176	2.591	1.23E+54	...	9.75E+30	93	48	VLA	1
080913	8	6.733	6.46E+52	...	4.07E+31	111	51	VLA	1
081024	2	$8.1^{+150}_{-7.7} \times 10^{-5}$...	<68	52	VLA	1,2
081118	49	2.58	2.82E+52	...	1.25E+31	<50	60	VLA	1
081126	58	24	64	VLA	1
081203A	223	2.05	3.47E+53	...	5.57E+30	76	54	VLA	1
081222	33	2.77	3.54E+53	...	6.24E+30	54	53	VLA	1
090102	29	1.547	1.99E+53	...	4.22E+30	91	49	VLA	1
090205	9	4.65	2.95E+52	...	4.91E+30	21	47	VLA	1
090429B	5.5	9.4	5.56E+52	...	2.93E+31	55	37	VLA	1
090809	8	2.737	1.39E+52	...	9.09E+29	8	39	VLA	1
090812	75	2.452	4.40E+53	...	5.99E+30	104	43	VLA	1
100420	48	<20	24	17	EVLA	1
100528A	25	<48	46	EVLA	1
101112A	35	149	54	EVLA	1
110106B	25	0.618	3.05E+52	...	4.16E+29	<21	24	EVLA	1
110731A	38.8	2.83	1.18E+54	...	3.82E+30	32	21	EVLA	1
120305A	0.1	260±90	110	AMI	8,9
120311A	3.5	210±80	80	AMI	8,9
120324A	118	110±70	90	AMI	8,9
120308A	60.6	80±50	60	AMI	8,9
120403A	1.25	190±100	90	AMI	8,9
120404A	38.7	2.876	6.71E+31	330±1090	100	AMI	8,9
120422A	5.35	0.28	4.40E+49	...	1.79E+28	30±30	410	AMI	8,9
120521C	26.7	150±250	130	AMI	8,9
120711B	60	230±60	80	AMI	8,9
120722A	42.4	670±1090	510	AMI	8,9
120724A	72.8	1.48	6.02E+51	...	4.30E+30	80±70	350	AMI	8,9
120729A	71.5	0.8	2.30E+52	...	2.56E+30	180±100	100	AMI	8,9
120802A	50	3.796	1.40E+32	20±20	130	AMI	8,9
120803B	37.5	210±110	120	AMI	8,9
120805A	48	370±140	170	AMI	8,9
120811C	26.8	2.671	8.80E+52	...	1.86E+31	350±300	440	AMI	8,9
120816A	7.6	440±730	190	AMI	8,9
120819A	71	120±140	210	AMI	8,9
120907A	16.9	0.97	3.46E+30	60±50	110	AMI	8,9
120911A	17.8	100±50	90	AMI	8,9
120913A	30.1	160±80	70	AMI	8,9
120923A	27.2	50±60	100	AMI	8,9
120927A	43	210±100	160	AMI	8,9
121001A	147	190±130	230	AMI	8,9
121011A	75.6	190±100	150	AMI	8,9
121017A	4.2	310±870	150	AMI	8,9
121028A	3.8	20±20	90	AMI	8,9
121108A	89	50±70	90	AMI	8,9
121125A	52.2	370±150	170	AMI	8,9
121202A	17.7	550±240	290	AMI	8,9
121211A	182	1.023	2.24E+30	20±20	70	AMI	8,9
121212A	6.8	70	AMI	8,9
130102A	77.5	110±220	60	AMI	8,9
130122A	64	10±10	70	AMI	8,9
130131A	51.6	60±40	70	AMI	8,9
130131B	4.3	2.539	1.02E+31	200±360	160	AMI	8,9
130327A	9	50±40	90	AMI	8,9
130418A	300	1.218	6.30E+52	...	2.76E+30	180±100	130	AMI	8,9
130420A	123.5	1.297	6.20E+52	...	2.74E+30	160±100	120	AMI	8,9
130420B	10.2	260±90	100	AMI	8,9
130502A	3	300±180	180	AMI	8,9
130505A	88	2.27	3.80E+54	...	1.03E+31	40±30	110	AMI	8,9
130511A	5.43	1.3	2.69E+31	780±1800	390	AMI	8,9

Table 2: Physical parameters of radio-quiet GRBs

GRB	T_{90} (s)	z	$E_{\gamma,iso}$ (erg)	n (cm^{-3})	$L_{\nu,p}$ (erg/s/Hz)	$f_{p,radio}$ (μJy)	RMS (μJy)	Radio Telescope	reference
130514A	204	3.6	4.95E+53	1310	AMI	8,9
130521A	11	220±520	110	AMI	8,9
130603B	0.18	0.356	2.10E+51	...	6.11E+29	90±50	60	AMI	8,9
130609A	7	90±60	90	AMI	8,9
130610A	46.4	2.092	5.78E+52	...	1.06E+31	140±70	100	AMI	8,9
130701A	4.38	1.155	2.10E+52	...	4.75E+30	170±70	70	AMI	8,9
130806A	640±2470	150	AMI	8,9
130829A	42.56	20±20	110	AMI	8,9
130831A	32.5	0.479	4.60E+51	...	1.37E+30	120±70	70	AMI	8,9
130912A	0.28	40±50	50	AMI	8,9
131002A	55.59	170±80	90	AMI	8,9
131127A	92.1	30±20	70	AMI	8,9
131128A	3	70±50	70	AMI	8,9
140103A	17.3	50±70	40	AMI	8,9
140114A	139.7	90±60	60	AMI	8,9
140129B	1.36	1.5	6.17E+30	50±30	40	AMI	8,9
140206A	93.6	2.74	2.78E+54	...	2.96E+31	180±80	90	AMI	8,9
140211A	89.4	100±30	40	AMI	8,9
140311B	70	20±30	60	AMI	8,9
140419A	94.7	3.956	1.90E+52	...	3.98E+31	100±50	60	AMI	8,9
140428A	17.42	4.7	2.61E+31	100±40	40	AMI	8,9
140502A	16.9	500±1750	60	AMI	8,9
140508A	44.3	1.03	2.10E+53	...	2.50E+30	80±40	50	AMI	8,9
140515A	23.4	6.32	5.38E+52	460±960	120	AMI	8,9
140516A	0.19	170±90	70	AMI	8,9
140518A	60.5	4.707	5.98E+52	...	4.51E+31	80±40	40	AMI	8,9
140521A	9.88	120±90	40	AMI	8,9
140623A	140±40	50	AMI	8,9
140709B	155	10±10	60	AMI	8,9
140710A	3.52	0.558	5.68E+29	80±50	70	AMI	8,9
140801A	7	1.32	4.90E+52	...	4.51E+31	140±50	50	AMI	8,9
140817A	244	20±20	50	AMI	8,9
140824A	3.09	80±50	90	AMI	8,9
140907A	79.2	1.21	2.71E+52	...	2.12E+30	140±100	110	AMI	8,9
140930B	40±30	50	AMI	8,9
141005A	4.34	270±900	70	AMI	8,9
141026A	146	3.35	5.60E+31	70±40	40	AMI	8,9
141031B	16	50±30	40	AMI	8,9
141130A	62.9	50	AMI	8,9
141220A	7.21	1.3195	2.29E+52	...	2.82E+30	20±30	40	AMI	8,9
141225A	40.24	0.915	8.59E+51	...	1.65E+30	30±30	150	AMI	8,9
150101A	0.06	80	AMI	8,9
150120A	1.2	0.46	1.90E+50	...	8.73E+29	50±30	40	AMI	8,9
150211A	13.6	80±40	50	AMI	8,9
150212A	11.4	370±1810	40	AMI	8,9
150302A	23.74	40	AMI	8,9
150309A	242	70±30	40	AMI	8,9
150314A	14.79	1.758	6.70E+53	...	9.17E+30	110±60	70	AMI	8,9
150317A	23.29	80±40	40	AMI	8,9
150323A	149.6	0.593	1.00E+52	...	5.59E+29	30±20	40	AMI	8,9
150323C	159.4	10±10	50	AMI	8,9

Note. In Column 1, ★ presents the SN/GRB. The peak flux density in Column 7 is upper limit. References are given in order for duration time(T_{90}), redshift(z), isotropic equivalent energy($E_{\gamma,iso}$) and medium density(n), respectively. [1]Chandra et al. (2012); [2]Fong et al. (2015); [3]Cusumano et al. (2007); [4]Tashiro M.S., et al. (2007); [5]Ghisellini et al. (2009); [6]de Ugarte Postigo et al (2007); [7]Bloom et al. (2003); [8]https://gcn.gsfc.nasa.gov/gcn3_archive.html; [9]Anderson et al. (2018).

Table 3: Physical parameters of radio-none GRBs

GRB	T_{90} (s)	z	$E_{\gamma,iso}$ (erg)	n (cm^{-3})	Radio Telescope	reference
970111	31	VLA	1
970402	105	ATCA	1
970616	200	VLA	1
970815	130	VLA	1
971227	7	VLA	1
980109	20	ATCA	1
980326	9	0.9	5.60E+51	...	VLA	1
980515	15	ATCA	1
981220	15	VLA	1
990217	ATCA	-
990520	10	VLA	1
990627	59	ATCA	1
990704	23	VLA	1
991014	3	VLA	1
991106	VLA	-
000115	15	VLA	1
000126	70	VLA	1
000214	115	0.47	8.00E+51	...	ATCA	1
000226	131	VLA	1
000301A	6	VLA	1
000315	60	VLA	1
000326	2	VLA	1
000424	VLA	-
000519	15	VLA	1
000528	80	VLA	1
000529	4	ATCA	1
000604	15	VLA	1
000607	0.2	VLA	1
000615A	12	VLA	1
000620	15	VLA	1
000727	10	VLA	1
000801	30	VLA	1
000812	80	VLA	1
000830	9	VLA	1
001025B	0.3	VLA	1
001109	60	VLA	1
001204	0.5	VLA	1
010119	0.2	VLA	1
010213	34	VLA	1
010214	15	VLA	1
010220	40	VLA	1
010728	8	VLA	1
011130	<3	VLA	1
020127	26	1.9	3.57E+52	...	VLA	1
020321	70	ATCA	1
020322	75	VLA	1
020331	75	VLA	1
020409B	VLA	-
020427	66	ATCA	1
020525	25	VLA	1
020531	1	1	VLA	1
021008	30	VLA	1
021020	20	VLA	1
021125	25	VLA	1
021201	0.3	VLA	1
021219	6	VLA	1
030306	20	VLA	1
030324	16	VLA	1
030528	84	0.782	3.04E+52	...	VLA	1
031111	10	VLA	1
040223	258	VLA	1
040701	60	0.21	8.02E+49	...	VLA	1
040827	49	VLA	1
040912	127	1.563	1.65E+51	...	VLA	1

Table 3: Physical parameters of radio-none GRBs

GRB	T_{90} (s)	z	$E_{\gamma,iso}$ (erg)	n (cm^{-3})	Radio Telescope	reference
040916	450	VLA	1
040924	5	0.859	1.10E+52	...	VLA	1
041006	25	0.716	3.50E+52	...	VLA	1
041218	60	VLA	1
050117A	167	VLA	1
050124	4	VLA	1
050126	25	1.29	8.00E+51	...	VLA	1
050128	19	VLA	1
050202	0.3	VLA	1
050319	153	3.24	4.60E+52	1.00E-08	VLA	1,3
050410	43	VLA	1
050412	27	VLA	1
050421	15	VLA	1
050509B	0.07	0.225	2.40E+48	...	VLA	1
050520	80	VLA	1
050522	15	VLA	1
050709	0.07	0.161	1.00E+51	$1^{+0.5}_{-0.4}$	VLA	1,2
050712	52	VLA	1
050714B	54	VLA	1
050803	88	VLA	1
050813	0.5	0.72	1.50E+50	...	VLA	1
050906	0.3	VLA	1
050911	16.2	0.165	2.69E+49	...	VLA	1
050922B	151	VLA	1
051006	35	VLA	1
051008	280	VLA	1
051016A	23	VLA	1
051103	0.2	VLA	1
051105A	0.09	VLA	1
051114	VLA	-
051117A	136	VLA	1
051117B	9	VLA	1
060110	26	VLA	1
060123	900	1.099	VLA	1
060206	8	4.05	4.07E+52	2	VLA	1,3
060210	255	3.91	4.20E+53	1.00E-08	VLA	1,3
060213	60	VLA	1
060313	0.7	$0.0033^{+1}_{-0.5}$	VLA	1,2
060421	12	VLA	1
060428B	58	VLA	1
060502B	0.13	0.287	3.00E+49	...	VLA	1
060505	4	0.089	4.37E+49	...	VLA	1
070306	210	1.497	6.00E+52	...	VLA	1
070518	5.5	VLA	1
070721B	32	3.63	3.13E+53	...	VLA	1
070724B	0.4	0.457	2.45E+49	$1.90^{+12}_{-1.6} \times 10^{-05}$	VLA	1,2
070923	0.2	VLA	1
071018	288	VLA	1
071112B	0.3	VLA	1
080120	15	VLA	1
080723B	95	ATCA	1
081024B	0.8	VLA	1
090417A	0.07	VLA	1
090417B	283	0.345	1.10E+51	...	VLA	1
100424A	104	2.465	EVLA	1
110721A	EVLA	-

Note. References are given in order for duration time(T_{90}), redshift(z), isotropic equivalent energy($E_{\gamma,iso}$) and medium density(n), respectively. [1]Chandra et al. (2012); [2]Fong et al. (2015); [3]Ghisellini et al. (2009)

Table 4. Statistical parameters of the distributions of z , T_{int} and $E_{\gamma,iso}$

sample	$\langle \log z \rangle$	$\sigma_{\log z}$	χ^2/dof	$\langle \log E_{\gamma,iso} \rangle$	$\sigma_{\log E_{\gamma,iso}}$	χ^2/dof	$\langle \log T_{int} \rangle$	$\sigma_{\log T_{int}}$	χ^2/dof
radio-loud(N=100)	0.18±0.014	0.69±0.031	1.84	53.0±0.04	1.80±0.09	1.94	1.48±0.02	0.86±0.04	1.72
radio-quiet(N=82)	0.16±0.01	0.70±0.025	1.054	52.33±0.029	1.76±0.063	0.85	1.08±0.02	1.06±0.048	1.82
radio-none(N=25)	-0.12	0.48	–	51.36	1.46	–	0.8	1.13	–

Table 5: The relevant parameters of K-S tests

Fig. †	N_1	N_2	D	P	$D_\alpha(N_1, N_2)$	Note ‡
1L	84 ^a	63 ^b	0.88	3.84×10^{-19}	0.23	rejected
1R	45 ^a	74 ^b	0.71	3.87×10^{-14}	0.26	rejected
2L	31 ^c	46 ^d	0.26	0.17	0.32	accepted
2L	46 ^d	48 ^e	0.33	8.5×10^{-3}	0.28	rejected
2L	31 ^c	48 ^e	0.41	2.5×10^{-4}	0.31	rejected
2R	31 ^c	43 ^d	0.23	0.26	0.32	accepted
2R	43 ^d	45 ^e	0.40	1×10^{-4}	0.29	rejected
2R	31 ^c	45 ^e	0.35	2.7×10^{-2}	0.32	rejected
3L	77 ^f	48 ^e	0.34	1×10^{-3}	0.25	rejected
3L	77 ^f	25^g	0.30	5×10^{-2}	0.31	rejected
3L	48 ^e	25 ^g	0.23	0.24	0.33	accepted
3L	21 ^h	34 ⁱ	0.30	0.15	0.37	accepted
3R	74 ^f	45 ^e	0.32	3.9×10^{-4}	0.26	rejected
3R	74 ^f	25 ^g	0.50	7.7×10^{-5}	0.31	rejected
3R	45 ^e	25 ^g	0.35	3.2×10^{-2}	0.34	rejected
3R	21 ^h	34 ⁱ	0.25	0.31	0.38	accepted
4	25 ^f	21 ^e	0.31	0.19	0.40	accepted
6	34 ^f	15 ^e	0.49	1.4×10^{-2}	0.45	rejected
7L	79 ^f	48 ^e	0.40	6.6×10^{-5}	0.25	rejected
7R	21 ^h	31 ⁱ	0.27	0.27	0.38	accepted

Note: N_1 and N_2 are two sample sizes. D is the K-S test statistic with a P value showing whether the two samples are taken from the same parent distribution. $D_\alpha(N_1, N_2)$ is the critical value in contrast with D for a significant level (SL) of $\alpha = 0.05$. The diverse samples characterized by whether the radio afterglows are detected or not are denoted by ^a for detection, ^b for upper limit, ^c for radio-loud I, ^d for radio-loud II, ^e for radio-quiet, ^f for radio-loud all, ^g for radio-none, ^h for AMI radio-loud and ⁱ for AMI radio-quiet.

† The capital letters represent the right (R) and left (L) panels in the corresponding figures.

‡ The bold face indicates those sample pairs with poor K-S test in a lower confidence level.

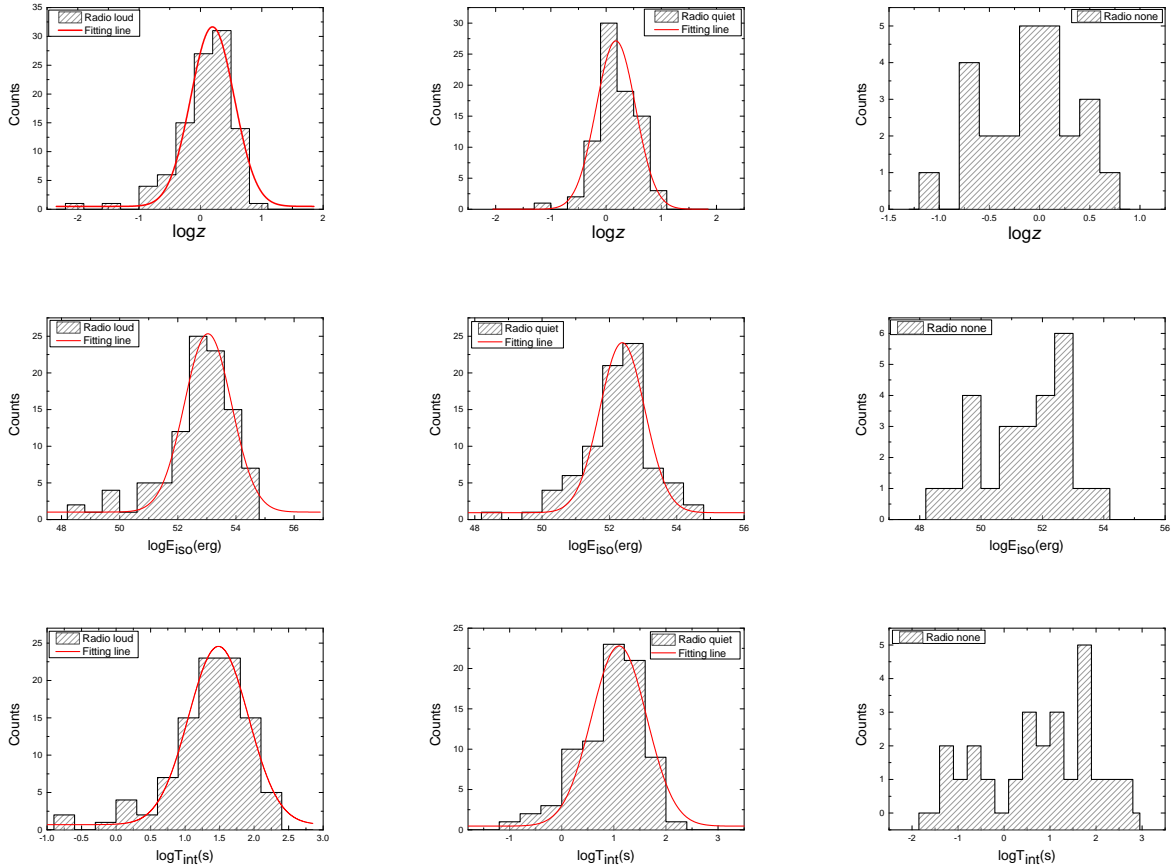


Figure A1. The histograms of z , $E_{\gamma,iso}$ and T_{int} for the radio-loud, radio-quiet and radio-none samples, respectively. The solid lines represent the best fit with a Gaussian function.

APPENDIX A: COMPARISONS OF TIMESCALES AND ENERGIES BETWEEN DIFFERENT RADIO-SELECTED GRBS

Here, we combine the VLA-based and the AMI GRBs to expand our sample and explore how the basic parameters of three radio-selected GRBs with known redshift are distributed. In total, 100 radio-loud, 81 radio-quiet and 25 radio-none bursts have been included and compared in Figure A1. Interestingly, the mean values of z , T_{int} and $E_{\gamma,iso}$ become smaller and smaller and are ranked in order for radio-loud, radio-quiet and radio-none GRBs. More importantly, this implies that radio-none GRBs with the lower γ -ray energy output and the shorter intrinsic duration time often occur in the nearby universe in contrast with other two kinds of GRBs with radio afterglows. However, only 24% of radio-none sources belong to short GRBs, which hints that a significant fraction of long GRBs without any radio detections have lower values of T_{int} and $E_{\gamma,iso}$. The new type of long GRBs is obviously different from most SN-associated GRBs with bright radio afterglow but lower $E_{\gamma,iso}$ as shown in Figure 9.

This paper has been typeset from a \LaTeX file prepared by the author.